

# Glass vs Backsheet: Deconvoluting the Role of Moisture in Power Loss in Silicon Photovoltaics with Correlated Imaging during Accelerated Testing

Rishi E. Kumar<sup>1</sup>, Guillaume von Gastrow<sup>1</sup>, Nicholas Theut<sup>2</sup>, April M. Jeffries<sup>2</sup>, Tala Sidawi<sup>1</sup>, Angel Ha<sup>1</sup>, Flavia DePlachett<sup>1</sup>, Hugo Moctezuma-Andraca<sup>1</sup>, Seth Donaldson<sup>1</sup>, Mariana I. Bertoni<sup>2</sup>, David P. Fenning<sup>1</sup>

<sup>1</sup> - University of California San Diego, La Jolla, CA, 92093, USA

<sup>2</sup> - Arizona State University, Tempe, AZ, 85281, USA

**Abstract**—Moisture ingress is an established issue for photovoltaic module durability. Durability studies that probe moisture effects typically evaluate performance losses at the module level, attributing global power losses to the overall humidity condition of the test environment while leaving local module behavior unknown. We leverage our recently published water reflectometry detection (WaRD) method and biased photoluminescence imaging to spatially correlate moisture content and cell performance over 2500 hours of damp heat testing. These tests, carried out on glass-glass and glass-backsheet mini-modules at multiple temperatures and humidities, reveal two dominant modes of local cell performance loss - acute finger interruptions and cell-wide “background” series resistance increase. Finger interruptions occur earliest in glass-glass modules and at dry conditions. We do not observe any signs of contact corrosion at the front side in either module type. Still, glass-backsheet modules show a unique increase in series resistance at high humidities, suggesting a mechanism at the back contact. Overall, our results point to the humidity level of installation climate as a driving variable in selection of the bottom module layer.

**Index Terms**—Silicon, Moisture, Durability, Degradation, Cracks, Power Loss

## I. INTRODUCTION

Water has been implicated in the degradation of photovoltaic modules by a variety of mechanisms, ranging from encapsulant yellowing and delamination to contact corrosion. Large surveys of fielded modules have identified encapsulant degradation, cracking, and interconnect corrosion as primary failure modes, with it being suggested that up to 90% of field failures arise from moisture-related issues [1], [2]. Studies of moisture-induced degradation generally track module power generation over time under exposure to outdoor or accelerated test conditions, linking performance loss of the entire module to its environment [3]–[5]. While module power output is the ultimate performance metric, it does not offer much insight as to the contributions of individual degradation modes to the net power loss, or to the specific role that moisture plays in each of these modes. A closer look at local cell degradation can be had by imaging techniques, revealing cracks and electrical defects [5], [6]. Local moisture content, however, has remained largely

a hidden variable, especially at a resolution at all comparable to that of imaging techniques.

Most studies of moisture effects on silicon PV durability fall under one of two categories - macroscopic studies of entire modules under accelerated or outdoor testing, or *ex-situ* testing of module components under conditions designed to simulate humidity exposure in the field. Macroscopic studies often track the current-voltage (IV) characteristics in conjunction with one or more imaging modalities to provide insight to local module degradation mechanisms during environmental exposure. These modalities include photoluminescence to identify electronic defects in cells, electroluminescence for crack detection, infrared thermography for hot-spot detection, and ultraviolet fluorescence imaging to observe encapsulant degradation [7]–[10]. Such correlative studies are lacking for module moisture content, which has remained a largely hidden variable due to difficulty of measurement. Infrared imaging techniques have been demonstrated for moisture detection in photovoltaic materials, though they either rely on transmission measurements (and are thus inapplicable in modules) or remain qualitative [11]–[13]. Embedded humidity sensors placed within the module during lamination can provide accurate values of module moisture content, though they provide little to no spatial resolution and may cause the module behavior to change [14].

*Ex-situ* study of module components has been used to evaluate moisture affects in more easily controlled environments where water content can be assessed. Encapsulants are among the most heavily studied components, and the diffusivity and solubility of water, decomposition mechanisms, and mechanical properties of standard materials are well understood [15]–[19]. These values are used to simulate moisture effects on module durability, including ethylene vinyl acetate decomposition, moisture uptake rates, and predicted module performance [6], [15], [20]–[23]. Investigation of this kind are attractive for their rapid cycle of learning (relative to the  $\geq 2000$  hours typical of aging experiments), but cannot easily capture combined effects that may arise in operating conditions.

In this study, we combine our recently published method for optical quantification of module moisture content with biased photoluminescence imaging to correlate local water content

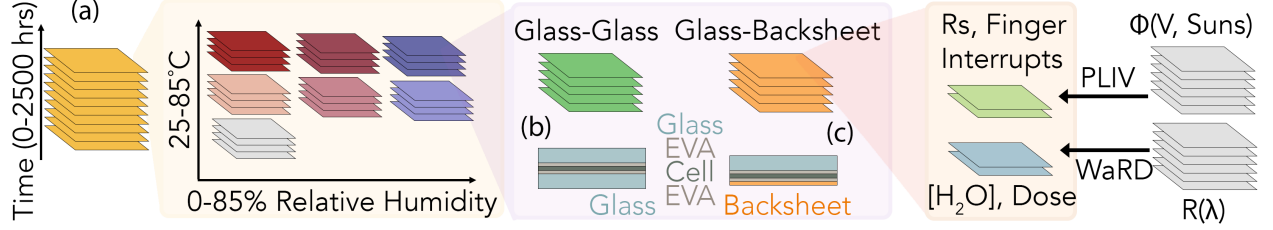


Fig. 1. (a) Schematic of the data flow in our study. Each square represents a single spatially-resolved dataset. Local cell parameters and moisture content are tracked for (b) glass-glass and (c) glass-backsheet modules at a range of temperatures and humidities across 2500 hours of environmental exposure

to local cell degradation at millimeter resolution [24], [25]. The water concentration and performance of modules with glass-glass (GG) and glass-backsheet (GB) bills of material (BOM) were tracked over 2500 hours of accelerated testing in conditions ranging across 25–85 °C and 0–85% RH. We find two dominant modes of performance loss, each involving local series resistance – acute interruption of finger connections, and “background” series resistance increase. Each mode shows a unique response between module types and varied sensitivity to moisture. The interrupts, many of which are confirmed to be cracks, are most prevalent in GG modules in dry conditions. Background resistance increases significantly more in GB modules than in GG modules at high humidity levels, suggesting moisture-induced degradation of the cell’s back contact. Our results suggest that in dry conditions, GB modules are preferred for their low rate of finger interruption, while in humid climates, GG modules are preferred to mitigate background series resistance losses.

## II. EXPERIMENTAL METHODS

### A. Sample Preparation

All tests are performed on 4.9x4.9 cm mini-modules made with silicon aluminum back surface field cells (Shenzhen Taihesheng Solar Energy Co., Ltd.). The cells are encapsulated into either glass-glass or glass-backsheet modules (Madico Protekt backsheets), which vary only in the bottom layer of the module stack (schematics in Figure 1b-c). All modules are laminated with ethylene vinyl acetate (3M EVA9100) at 145 °C for 18 minutes.

1) *Backsheet Ingress Sister Samples*: Sister GB modules were fabricated with the cell replaced by strips of aluminum foil spaced 10 mm apart. This allowed us to measure moisture concentration through the front glass at the edge of the foil strips (using the Water Reflectometry Detection method as described below), where the relevant diffusion path for moisture is directly through the backsheet. These sister modules were saturated with water at 85 °C, 85% RH. Their water content was then mapped at 45 minute intervals over 48 hours while being held at 85 °C in room conditions.

2) *Samples for Study of Metallization Corrosion*: Sister GB modules were fabricated with a strip of polytetrafluoroethylene (PTFE) embedded at the edge of the sample between the front of the cell and the EVA layer. This PTFE allows us to selectively delaminate the front cell/EVA interface with a 180°peel (0.5 kN Instron load cell), exposing the front of the cell for testing.

### B. Damp Heat Accelerated Tests

62 mini-modules are each subjected to one of seven environmental conditions - 0, 40, or 85% relative humidity (RH) at 65 or 85 °C, or 0% RH at 25 °C (Table I. Dry environments were maintained in either a nitrogen glovebox (0% RH) or a desiccator constantly purged with dry air ( $\leq 3\%$  RH). Samples are held in their environment for up to 3000 hours. Each module is characterized by a suite of techniques *ex-situ* weekly until 2184 hours (13 weeks), after which they are measured every other week.

TABLE I  
MINI-MODULE SAMPLES STUDIED UNDER DAMP-HEAT TESTING

Packaging	Temp. (°C)	Rel. Humidity (%)	# Samples
Glass-Backsheet	25	0	2
	65	0	3
	65	40	5
	85	85	5
	85	0	4
	85	40	5
Glass-Glass	25	0	3
	65	0	4
	65	40	6
	85	85	6
	85	0	4
	85	40	5
		85	5

### C. Current-Voltage Measurement

Standard current-voltage (IV) measurements are taken in a four-wire configuration under 1-sun illumination (Class ABA Newport solar simulator using either a Kepco BOP 20-20D-4866 or Keithley 2401).

### D. Spatial Quantification of Module Moisture Content

We use Water Reflectometry Detection (WaRD) to quantify the water content within a module’s front-side encapsulant layer by short-wave infrared (SWIR) reflectance [24]. Maps of module SWIR reflectance were taken with a mapping spectrophotometer consisting of a tunable laser (NKT Photonics Compact and Select), translation stages (Thorlabs LTS150), integrating sphere (Thorlabs IS200), InGaAs detectors (Thorlabs PDA10DT), and a lock-in amplifier (Stanford Research Systems SR830). Maps are acquired with 1 or 2 mm steps. All samples are measured in room conditions except those exposed to 85 °C, 85% RH, which are heated to 85 °C

during measurement to avoid moisture condensation effects [24]. To reduce mapping time to 45 minutes per module, we acquire reflectance at just 3 critical wavelengths (at the 1730 nm ethylene vinyl acetate stretching mode, at the 1872 nm isosbestic point as a baseline metric, and at the 1902 nm water combination mode) at each point. Additional full spectra (151 distinct wavelengths) are acquired at 10 mm intervals in each direction. The background spectra extracted from each full measurement are interpolated and scaled to intersect the 1872 nm baseline reflectance at each 3-wavelength point. Using this approach, we find that water measurements taken with the 3-wavelength method match those of the original full 151-wavelength sampling ( $R^2 > 0.95$ ).

#### E. Spatial Determination of Cell Parameters

We employ photoluminescence current-voltage (PLIV) imaging to spatially resolve the cell parameters of each mini-module using a two-diode cell model (series resistance, saturation currents, and illumination current, no shunt) at a resolution of  $\leq 100 \mu\text{m}$  [25]. All samples are measured in room conditions. The top glass of each cell is cleaned with isopropyl alcohol (IPA) immediately prior to measurement to avoid image artifacts from glass fouling. Images are acquired by an InGaAs camera (FLIR A6251sc). A four-quadrant power supply (Kepco BOP 20-20D-4866) is used to apply bias to and measure current from cells during PLIV. A 15 watt 808 nm laser (Jenoptik JOLD-30-FC18) and optical diffuser are used to illuminate cells with  $>95\%$  homogeneity across the cell area. Samples are maintained at 25 °C during measurement by a thermoelectric cooler (TE Technology CP-040HT). The short-circuit current ( $J_{sc}$ ), open-circuit voltage ( $V_{oc}$ ), and maximum-power point voltage ( $V_{mpp}$ ) from the JV measurement are used to determine PLIV measurement parameters. Images are acquired at all combinations of electrical bias (in 100 mV steps from  $V_{mpp}$  to  $V_{oc}$ ) and incident photon flux (in steps of 0.2 suns from 0 to 1 sun equivalent illumination). 1-sun equivalent illumination is taken as the laser current at which the short-circuit current generated by the cell under the laser matches that from the JV measurement. An additional “background” image, taken with no illumination or applied bias, is subtracted from all other images. PLIV is carried out at room conditions.

#### F. Identification of Finger Interruptions

Forward-bias electroluminescence at  $V_{oc}$  (FBEL) images are acquired during the PLIV routine. Local Otsu thresholding is used to binarize FBEL images, yielding an “isolation mask” where 1 represents electrically isolated regions of the cell [26]. A similar treatment to a luminescence image at  $V_{oc}$  and 1-sun illumination yields a “finger mask” and “busbar mask”. The union of the finger and isolation masks yields an “interruption mask” where 1 represents portions of fingers that are electrically interrupted from the busbar (interrupt mask). The “interruption mask” points with the shortest distance to the busbar are identified as finger interruptions. Results were manually pruned to remove false positives (< 3%) from artifacts such as camera obstructions or glass fouling. We note that, along an already interrupted finger, subsequent interruptions

further from the busbar will not provide additional contrast by FBEL and are therefore undetectable in our scheme.

#### G. Registration of WaRD and PLIV Data

Module orientation varies slightly from week to week and between PLIV and WaRD hardware. In each image, the same four module corners are manually located and used to align the image to a common orientation by rigid transformation. As maps of module moisture content and cell parameters are acquired at different spatial resolutions, a nearest-neighbor approach was used to relate the coarse WaRD maps to the PLIV data.

#### H. Raman Mapping of Contact Corrosion

The sister GB modules described in section II-A2 were exposed to 85 °C, 85% RH for up to 1000 hours, then peeled to expose the front side of their cells. Raman spectra were taken over the cell metallization near the center of the cell. Progress of corrosion reactions were monitored by Raman spectroscopy mapping on samples that had undergone different environmental exposures [27]. Raman spectra were taken from 0 to 1200  $\text{cm}^{-1}$  by a Renishaw Confocal InVia Raman system (backscatter geometry, 100 mW 532 nm laser excitation source, 50x objective, 1.5  $\mu\text{m}$  spot size). A 1250  $\mu\text{m} \times 250 \mu\text{m}$  region above the busbar of each sample was mapped with a step size of 50  $\mu\text{m}$ . For each sample, these 125 spectra were normalized to the intensity of the silver acetate vibrational mode (145  $\text{cm}^{-1}$ ) and averaged [27].

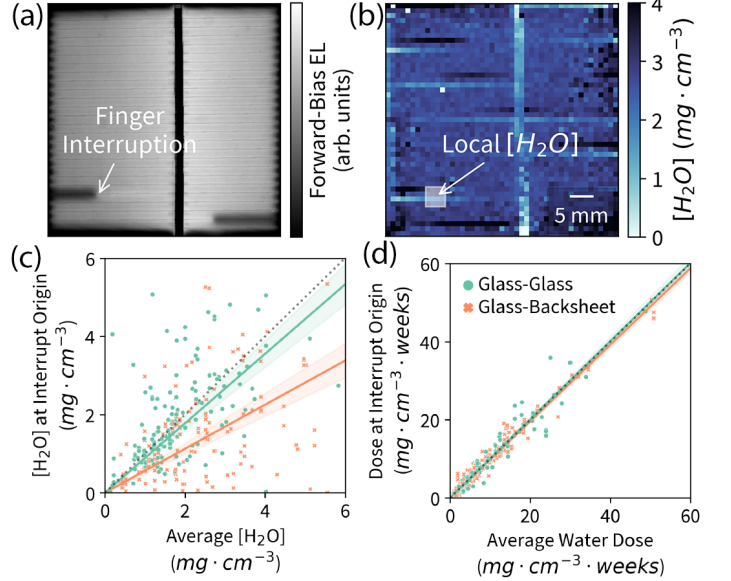


Fig. 2. Example pair of (a) electroluminescence and (b) water content maps for a glass-backsheet module exposed to 85 °C, 85% RH for 670 hours. (c) Water concentration and (d) dose are compared between the interrupt location and the rest of the cell area across all environmental conditions. The dotted lines indicate equivalent water content/dose, the solid lines indicate linear fits, and the shaded bands indicate 95% confidence intervals.

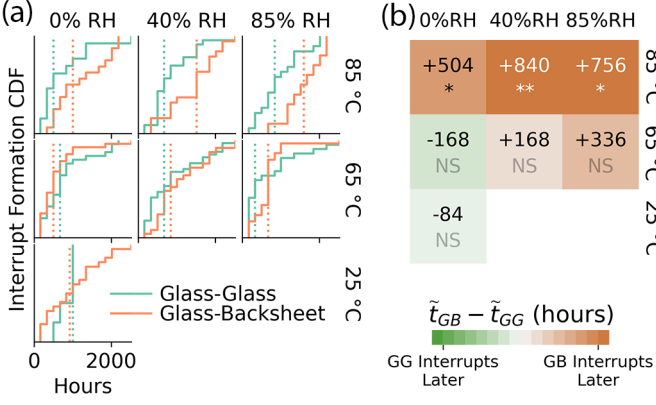


Fig. 3. (a) Cumulative distribution of interrupt formations for glass-glass and glass-backsheet modules at each environmental condition. Dashed lines indicate median times to interruption. (b) The difference in median time ( $\tilde{t}$ ) to interrupt formation between the two architectures at each environmental condition. Asterisks represent statistical significance in comparison across the two architectures at each condition (\*\* =  $p < 0.01$ , \* =  $p < 0.05$ , NS =  $p \geq 0.05$ ).

### III. RESULTS AND DISCUSSION

#### A. Moisture Saturates Rapidly at the Back Side of Glass-Backsheet Modules

WaRD maps on GB test modules (constructed without a cell to allow WaRD measurements to see water ingress through the backsheet) find that moisture content of the back side saturates in under 24 hours at 85 °C. WaRD maps on standard GG and GB mini-modules show that the front side reaches moisture saturation above the center of the cells after in about 500 hours at 85 °C. This rate of front side ingress is also representative of the back side in symmetric GG modules. Together, these experiments demonstrate that the back side of the GB modules reaches saturation roughly 3 weeks earlier than the GG modules.

#### B. Finger Interruptions Form in Drier Regions of Glass-Backsheet Modules

Through weekly FBEL and WaRD imaging of each sample, we extract the location, timing, water concentration, and accumulated water dose at each interruption. (Figure 2a-b). Water dose accumulated by time  $t_n$  is defined by  $D(x, y, t_n) = \sum_{i=0}^n c(x, y, t_i)$ , where  $D$ ,  $t$ , and  $c$  represent dose, time in environmental exposure, and water concentration for coordinates  $(x, y)$  on the cell area. We exclude “day zero” interruptions (present in the as-fabricated modules) from our analyses of interrupt location and timing.

We evaluate the effect of local water concentration and dose on the formation of finger interruptions by comparing the water content in the immediate vicinity (within 2 mm) of the interrupt origin to the average water content across the module. The local and module-average contents are compared by linear regressions (Figure 2c-d) and Mann-Whitney U Tests [28]. GB modules formed interruptions in drier points within the module ( $p$ -value < 0.01, Fig. 2c). By contrast, interrupt origins in GG modules are not drier than the rest of the module ( $p = 0.51$ ). Local dose did not differ from average dose within

either module type ( $p = 0.90$  for GG,  $p = 0.70$  for GB). Additionally, the local dose around interrupts did not differ across module types ( $p = 0.41$ ).

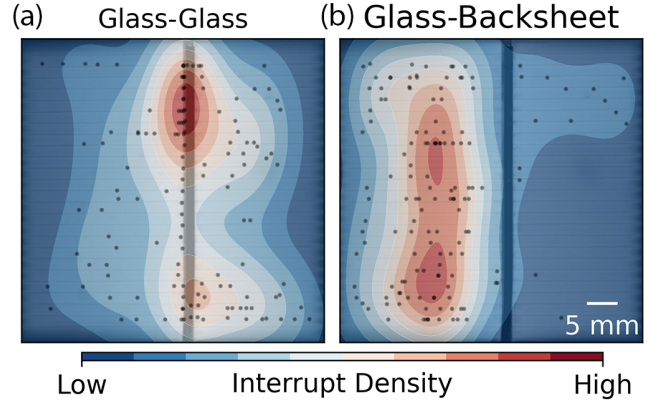


Fig. 4. The spatial distribution of interrupts in (a) glass-glass and (b) glass-backsheet modules across all environmental conditions.

The accumulation of new interruptions over time in GG and GB modules is shown at each tested environmental condition in Figure 3a, where each curve describes the rate at which the total population of interruptions within each condition and BOM occur over 2500 hours of damp heat testing. These populations of interruption timings are compared across module types in two ways: the median timings (shown by the dashed lines in Figure 3a), and Mann-Whitney U Tests to evaluate whether these differences are statistically significant. GG modules interrupt earlier than GB modules at our highest tested temperature of 85 °C, with statistical significance at all humidity levels (Figure 3b). Interestingly, increasing humidity seems to delay the onset of interruptions, as the median time to interruption is shorter in the driest samples. This is especially the case in GB modules, and the gap between GG and GB times to interruption grows with increasing humidity at each temperature.

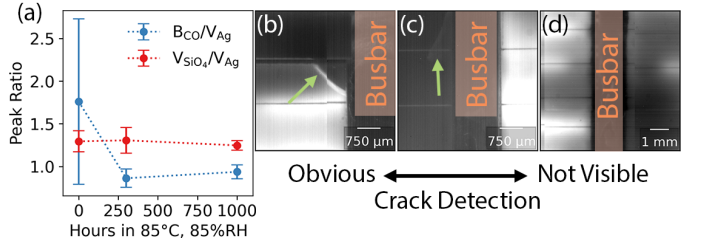


Fig. 5. (a) Evolution of Raman vibrational modes indicative of silver contact corrosion at the busbar of GG modules over 1000 hours of exposure to 85 °C, 85% RH. (b-d) Representative high-resolution forward-bias electroluminescence images at finger interrupt origins. Green arrows indicate cracks when they are visible.

#### C. Glass-Glass Modules Form Interruptions at the Busbar

We find that finger interruptions in GG and GB modules form in different characteristic module regions (Figure 4). GG modules form interruptions along the busbar, often near the module edge. GB modules, by contrast, tend to form interruptions

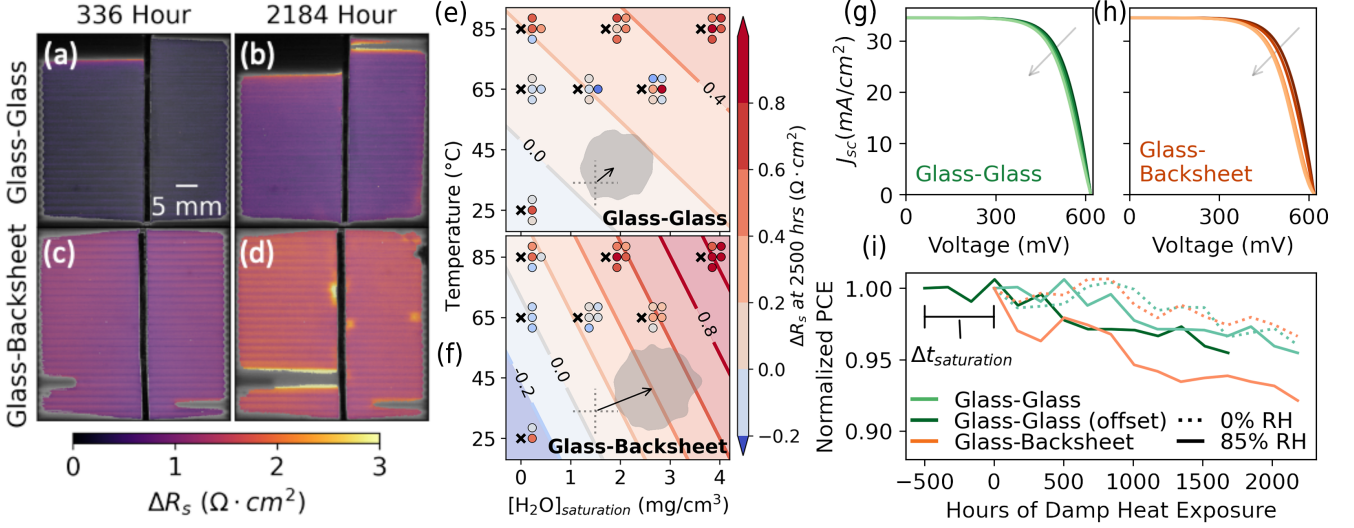


Fig. 6. Change in series resistance for representative (a-b) glass-glass and (c-d) glass-backsheet modules after exposure to 85 °C, 85% RH. The grayscale background depicts forward-bias electroluminescence, while the foreground shows series resistance in the uninterrupted area. Increase in background resistance as a function of temperature and saturated module water content for (e) glass-glass and (f) glass-backsheet modules after 2500 hours of accelerated testing. The black crosses indicate test conditions, while the adjacent circles denote  $R_s$  changes in individual modules at each test condition. The color bar is shared between the contours and circles. The inset vector shows the gradient of  $R_s$  change with respect to temperature and saturated module water content, and the shading indicates 95% confidence bounds for the gradient vector. Simulated current-voltage curves for (g) glass-glass and (h) glass-backsheet modules affected only by background series resistance. (i) Isolated power loss from background resistance. The “offset” GG data is shifted such that its moisture saturation time matches that of GB modules.

mid-finger, away from the busbar but not at the very edge of the module. The spatial distribution of interruptions within each module type does not vary across time or environmental condition.

#### D. No Evidence of Contact Corrosion

Raman spectra taken over the metallization near the center of cells extracted from GB mini-modules exposed to accelerated testing suggest that historical modes of contact corrosion are not occurring in these samples. Previous literature has established that in the event that the silver cell metallization is corroded by acetic acid generated from degradation of EVA encapsulant, the SiO<sub>4</sub> vibrational mode decreases in intensity while the C-O-Ag bending modes increases in intensity [27], [29], [30]. These changes are attributed to corrosion of the glass frit by acetic acid and the formation of silver acetate, respectively. We do not observe either of these changes in our modules after 1000 hours at 85 °C, 85% RH (5a).

High resolution FBEL imaging in the vicinity of interrupt origins shows at least some of the interrupts to be caused by cracks in the cell. Absence of a visible crack here is not sufficient to say that a crack is not present, as they may be too small for our camera to observe (the highest resolution of our imaging hardware is about 30  $\mu\text{m}$ ) or positioned as to not affect the metallization (on which the contrast mechanism of FBEL relies).

#### E. Background Series Resistance Increases More in Glass-Backsheet Modules

Setting aside the regions of modules affected by finger interruptions, GB modules exhibit a larger increase in series resistance than GG modules at all but 0% RH conditions. We

leverage the spatial characterization of cell parameters from PLIV and segmentation of finger interruptions from FBEL images to evaluate the uninterrupted “background” region of modules in isolation (Figure 6a-d). The grayscale background image in Figure 6a-d shows the raw FBEL image, and the purple-yellow foreground image shows the  $R_s$  map from PLIV plotted only in the “background” regions considered in subsequent analysis of background  $R_s$ . Degradation by background series resistance in particular differs between GG and GB samples, with GB samples suffering a greater increase in resistance at all but the driest conditions. To better quantify this difference, for each module type we fit a first order response surface

$$d_{R_s} = a + bT + c[H_2O],$$

where  $d_{R_s}$  is the change in series resistance after 2500 hours of environmental exposure, T is the temperature (°C), and  $[H_2O]$  is the saturation water content (mg/cm<sup>3</sup>) in the module for a given environment. Individual module changes in background series resistance and the fitted response surfaces are shown in

TABLE II  
BACKGROUND SERIES RESISTANCE RESPONSE SURFACES

Glass-Glass	Coefficient	Std. Err.	p-value	95% CI
a (constant)	-0.253	0.273	0.362	(-0.811, 0.306)
b (temperature)	0.005	0.004	0.211	(-0.003, 0.014)
c ( $[H_2O]$ )	0.083	0.055	0.143	(-0.03, 0.196)
Glass-Backsheet	Coefficient	Std. Err.	p-value	95% CI
a (constant)	-0.371	0.282	0.2	(-0.95, 0.209)
b (temperature)	0.006	0.004	0.152	(-0.002, 0.015)
c ( $[H_2O]$ )	<b>0.147</b>	<b>0.051</b>	<b>0.008</b>	<b>(0.042, 0.252)</b>

Figure 6e-f, and the numerical values and uncertainties of the response surfaces are given in Table II. Though some outlying samples render our parameter confidence intervals quite wide, we see with statistical significance that higher water content leads to greater background series resistance increases in GB modules.

We isolate the impact of background  $R_s$  on module power generation by simulating their current density-voltage (JV) curves by the same shuntless two-diode cell model used in PLIV fitting [25]. Cell parameters are initialized by fitting JV curves measured for each cell prior to environmental exposure. The average background  $R_s$  increase from PLIV is then added to the starting  $R_s$  while all other parameters are held constant, yielding simulated JV curves affected only by this degradation mode. Representative simulated curves for GG and GB modules over 2500 hours at 85 °C, 85% RH are shown in Fig. 6g-h, along with the power conversion efficiency (PCE) extracted from such curves for all modules at 85 °C, 85% RH in Figure 6i. By shifting the GG PCE trendline 500 hours earlier, we align the GG and GB data such that both reach moisture saturation at the back contact at roughly t=0 hours. Still, the GB modules suffer about twice the PCE loss from background resistance as GG modules. In a dry environment at the same 85 °C temperature, the two module types show nearly identical increases in background resistance.

#### F. Net Effects of Finger Interruptions and Background Resistance

The individual and net impacts of background  $R_s$  and finger interruptions were extracted for each individual module, and are shown in Figure 7. Losses from background  $R_s$  are calculated by JV curve simulation as discussed in section III-E. The impact of finger interruptions on PCE for each cell are estimated from the inactive area fraction seen via FBEL. The inactive area is scaled to an equivalent PCE loss by  $PCE_{norm} = 1 - 0.467 * Area_{inactive}$ . This relationship was empirically determined by a linear fit (RMSE=3%  $PCE_{norm}$ ) to observed inactive area and normalized PCE (from JV curves) from our GG modules. We fit GG modules alone as we observed the majority of their power losses to arise from finger interruptions, and a fit to GB modules would include large background resistance effects.

## IV. DISCUSSION

### A. Mechanical Properties of Module Packaging May Explain Finger Interruptions

Our forensic analysis of finger interruptions suggests that their primary cause is cell cracking. For many of our interruptions, these cracks are clearly visible in FBEL. For the others, the alternative explanation of contact corrosion seems unlikely as we do not observe Raman signatures of byproducts from corrosion of the metallization (at least within the first 1000 hours of exposure to 85°C, 85% RH, by which point 70% of GG and 32% of GB finger interruptions had formed). We speculate that the difference in location of interruptions between GG and GB modules may arise from the mechanical properties

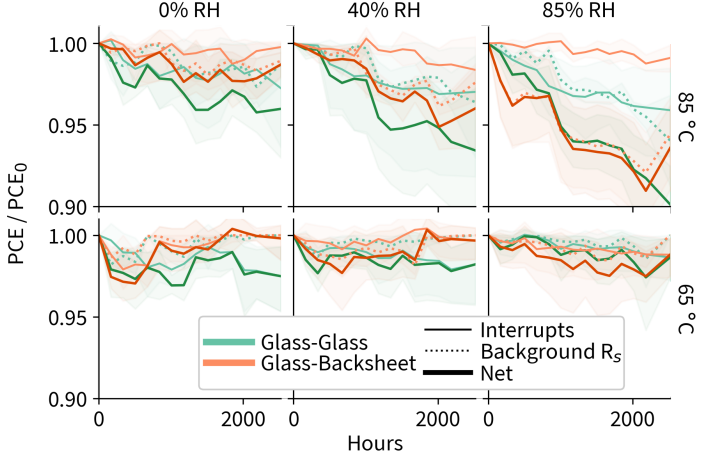


Fig. 7. The isolated impacts of finger interruptions and background series resistance on power conversion efficiency are shown for each elevated environmental condition. The net loss in power conversion efficiency is also shown.

of the module constructions. Previous studies found modules with stiffer encapsulants to generate larger stresses within the silicon cell [31], [32]. Additional reports find GG modules to generate larger stresses during lamination and thermal cycling than GB modules [33], [34]. Our observation of a high density of interruptions near the ends of the busbars in GG samples is consistent with reports of cracks formed during the interconnect soldering process [6], [35]. Lamination and tab soldering processes generate mechanical stresses in modules from coefficient of thermal expansion (CTE) mismatches between module components, and these stresses are most acute in the immediate vicinity of the interconnects [6], [32], [36]–[38]. The cause of mid-finger interruptions in GB samples is less clear, though we note that the combined thickness of the backsheet and back side ethylene-vinyl acetate layers in our modules thins from center to edge. Thicker polymer layers have been shown to reduce the fraction of total module mechanical stresses imparted across the cell [32].

We see that interruptions form earlier in drier conditions, and that interruptions in GB modules tend to form in drier parts of the module. Previous reports find the shear storage modulus of solar encapsulants to lessen with moisture exposure, attributed to plasticization of the polymers [17]. Stiffer (and, accordingly, drier) encapsulants impart more mechanical stresses on the cell, which would increase the chance of cracking [31], [39]. The magnitude of this plasticization effect varies dramatically across encapsulants. For EVA, a 63% increase in relative humidity is required to match the reduction in shear modulus of a 1 °C temperature increase. Interestingly, the shear storage modulus of polyvinyl fluoride-based backsheet (as used in our modules) was found to be 16 times more sensitive to moisture than that of EVA (just a 4% RH increase is equivalent to a temperature increase of 1 °C). Assuming that the finger interruptions we observe are from mechanical cracks in the cell, the greater plasticization of backsheets may be a contributing factor to the delayed formation of finger interruptions we observe in GB modules at high humidities. Future studies

aimed at colocation of module stresses and water content across environmental conditions and bills of material should be undertaken to investigate this moisture-driven mechanism of mechanical failure in modules.

### B. A Mode of Series Resistance Increase Unique to Glass-Backsheet

Background series resistance increases in uninterrupted cell regions are nearly twice as severe in GB modules than GG at the most aggressive humidity condition. Possible explanations for this result include faster moisture ingress through the backsheet leading to earlier degradation by the same mode, or a unique degradation mode between the backsheet and the cell which is not present in the GG modules. The moisture content at the back side of GB modules reaches saturation a full 500 hours earlier than GG at 85 °C. Even when accounting for this offset (for example comparing GB week 3 to GG week 6) the series resistance of GB modules remains higher, suggesting that the difference in time to water saturation is not a sufficient explanation for this issue (Figure 6h). In fact, the series resistance of our GG modules does not show much sensitivity to humidity at all, displaying essentially the same power loss from background resistance in 0% RH and 85% RH conditions at 85 °C (Figure 6h). In all scenarios, the front side of GB and GG modules should have identical moisture exposure. Together these observations implicate moisture as a reactant in some form of back-contact degradation mode unique to GB modules with Al-BSF cells. Future work is needed to check for a similar degradation mode in passivated emitter rear contact (PERC) cells in GB modules.

### C. Tailoring Module Packaging to Deployed Environment

The durability of the GG modules in this study is limited by finger interruptions, and the durability of GB modules by background  $R_s$  issues at high humidities. The results would suggest that GB modules would be preferred in drier climates, while GG modules would be best suited for humid climates. This stands in contrast to the conventional wisdom that a "breathable" backsheet is preferred in humid environments to allow moisture and acetic acid generated from EVA hydrolysis to escape the module [18], [40]. Modern cells with newer solder paste formulations may be less susceptible to contact corrosion via acetic acid, as demonstrated by the invariance of the  $R_s$  of the GG modules in this study to humidity and the absence of corrosion byproducts in Raman measurements. This is encouraging, as the market share of GG modules is projected to increase due to growing interest from grid installers in bifacial modules [41]. Further efforts to reduce cracking in GG modules are needed. Given that the majority of GG cracks originate at the busbar, technologies that aim to either reduce thermal stresses at the busbar during soldering [42] or to implement interconnect that avoid busbars altogether could be of interest.

## V. CONCLUSION

We have shown that moisture can be accessed as a dimension in correlative studies of module durability. Two primary

modes of cell degradation were tracked during durability testing using correlative imaging - finger interruptions and "background" series resistance. Finger interruptions occurred earlier in glass-glass modules than in glass-backsheet, and at drier conditions regardless of module architecture. Interrupts in glass-backsheet modules formed in drier parts of the module.

Background series resistance shows a strong sensitivity to humidity in glass-backsheet modules, in which raising relative humidity at 85 °C from 0 to 85% RH doubled the efficiency loss attributed specifically to this degradation mode (from 4 to 8% relative after 2500 hours). In contrast, we find that modern glass-glass modules are resilient to humidity-driven increases in series resistance. The performance of glass-glass modules is primarily limited by mechanical failures in the cell. To improve the operating lifespan of fielded modules, it will be important to understand the influence mechanical stress has on module durability.

Future WaRD-informed studies on fielded modules or in a fluctuating test environment designed to generate moisture gradients within the module may reveal further local influences of water on silicon module durability.

## REFERENCES

- [1] E. Annigoni, A. Virtuani, M. Caccivio, G. Friesen, D. Chianese, and C. Ballif, "35 years of photovoltaics: Analysis of the tiso-10-kw solar plant, lessons learnt in safety and performance—part 2," *Progress in Photovoltaics: Research and Applications*, vol. 27, no. 9, p. 760–778, 2019.
- [2] J. H. Wohlgemuth, D. W. Cunningham, P. Monus, J. Miller, and A. Nguyen, "Long term reliability of photovoltaic modules," in *Long term reliability of photovoltaic modules*, vol. 2006 IEEE 4th World Conference on Photovoltaic Energy Conference 2. IEEE, 2006, pp. 2050–2053.
- [3] D. C. Jordan and S. R. Kurtz, "Photovoltaic degradation rates—an analytical review," *Progress in photovoltaics: Research and Applications*, vol. 21, no. 1, p. 12–29, 2013.
- [4] W. Herrmann and N. Bogdanski, "Outdoor weathering of pv modules—effects of various climates and comparison with accelerated laboratory testing," in *Outdoor weathering of PV modules—effects of various climates and comparison with accelerated laboratory testing*, vol. 2011 37th IEEE Photovoltaic Specialists Conference. IEEE, 2011, pp. 002 305–002 311.
- [5] J. Zhu, M. Kochl, S. Hoffmann, K. A. Berger, S. Zamini, I. Bennett, E. Gerritsen, P. Malbranche, P. Pugliatti, A. Di Stefano, F. Aleo, D. Bertani, F. Paletta, F. Roca, G. Graditi, M. Pellegrino, O. Zubillaga, F. J. C. Iranzo, A. Pozza, T. Sample, and R. Gottschalg, "Changes of solar cell parameters during damp-heat exposure," *Progress in Photovoltaics: Research and Applications*, vol. 24, no. 10, p. 1346–1358, 2016.
- [6] L. Papargyri, M. Theristis, B. Kubicek, T. Krametz, C. Mayr, P. Papanastasiou, and G. E. Georghiou, "Modelling and experimental investigations of microcracks in crystalline silicon photovoltaics: A review," *Renewable Energy*, vol. 145, p. 2387–2408, 2020.
- [7] M. Owen-Bellini, D. B. Sulas-Kern, G. Perrin, H. North, S. Spataru, and P. Hacke, "Methods for in situ electroluminescence imaging of photovoltaic modules under varying environmental conditions," *IEEE Journal of Photovoltaics*, vol. 10, no. 5, p. 1254–1261, 2020.
- [8] D. B. Sulas-Kern, S. Johnston, M. Owen-Bellini, K. Terwilliger, J. Meydbray, L. Spinella, A. Sinha, L. T. Schelhas, and D. C. Jordan, "UV-fluorescence imaging of silicon pv modules after outdoor aging and accelerated stress testing," in *UV-Fluorescence Imaging of Silicon PV Modules After Outdoor Aging and Accelerated Stress Testing*, vol. 2020 47th IEEE Photovoltaic Specialists Conference (PVSC). IEEE, 2020, pp. 1444–1448.
- [9] R. Bhoopathy, O. Kunz, M. Juhl, T. Trupke, and Z. Hameiri, "Outdoor photoluminescence imaging of photovoltaic modules with sunlight excitation," *Progress in Photovoltaics: Research and Applications*, vol. 26, no. 1, p. 69–73, 2018.

- [10] J. Karas, L. Michaelson, K. Munoz, M. Jobayer Hossain, E. Schneller, K. O. Davis, S. Bowden, and A. Augusto, "Degradation of copper-plated silicon solar cells with damp heat stress," *Progress in Photovoltaics: Research and Applications*, vol. 28, no. 11, p. 1175–1186, 2020.
- [11] M. Bora, S. Pop, R. Schulze, M. Rowell, and D. Harwood, "Moisture content imaging in glass-glass and glass-backsheet photovoltaic mini-modules," in *Moisture content imaging in glass-glass and glass-backsheet photovoltaic mini-modules*, vol. 2020 47th IEEE Photovoltaic Specialists Conference (PVSC). IEEE, 2020, pp. 1485–1488.
- [12] M. Bora, V. Lordi, and J. B. Varley, "Water ingress mapping in photovoltaic module packaging materials," vol. 2018 IEEE 7th World Conference on Photovoltaic Energy Conversion, no. WCPEC, 2018, p. 1252–1254.
- [13] J. Hepp, A. Vetter, S. Langner, M. Woiton, G. Jovicic, K. Burlafinger, J. A. Hauch, C. Camus, H.-J. Egelhaaf, and C. J. Brabec, "Infrared absorption imaging of water ingress into the encapsulation of (opto-)electronic devices," *IEEE Journal of Photovoltaics*, vol. PP, p. 1–7, 2018.
- [14] M. Jankovec, F. Galliano, E. Annigoni, H. Y. Li, F. Sculati-Meillaud, L.-E. Perret-Aebi, C. Ballif, and M. Topic, "*italic\_in-situ/italic* monitoring of moisture ingress in pv modules using digital humidity sensors," *IEEE Journal of Photovoltaics*, vol. 6, no. 5, p. 1152–1159, 2016.
- [15] M. D. Kempe, "Modeling of rates of moisture ingress into photovoltaic modules," *Solar Energy Materials and Solar Cells*, vol. 90, no. 16, p. 2720–2738, 2006.
- [16] M. D. Kempe, G. J. Jorgensen, K. M. Terwilliger, T. J. McMahon, C. E. Kennedy, and T. T. Borek, "Acetic acid production and glass transition concerns with ethylene-vinyl acetate used in photovoltaic devices," *Solar Energy Materials and Solar Cells*, vol. 91, no. 4, p. 315–329, 2007.
- [17] N. Bosco, M. Springer, and X. He, "Viscoelastic material characterization and modeling of photovoltaic module packaging materials for direct finite-element method input," *IEEE Journal of Photovoltaics*, vol. 10, no. 5, p. 1424–1440, 2020.
- [18] G. Oreski, A. Mihaljevic, Y. Voronko, and G. C. Eder, "Acetic acid permeation through photovoltaic backsheets: Influence of the composition on the permeation rate," *Polymer Testing*, vol. 60, 2017.
- [19] A. Mannodi-Kanakkithodi, R. Kumar, D. Fenning, and M. Chan, "First principles modeling of polymer encapsulant degradation in si photovoltaic modules," *Phys Chem Chem Phys*, 2021.
- [20] O. Hasan and A. F. Arif, "Performance and life prediction model for photovoltaic modules: Effect of encapsulant constitutive behavior," *Solar Energy Materials and Solar Cells*, vol. 122, p. 75–87, 2014.
- [21] P. Hacke, S. Spataru, K. Terwilliger, G. Perrin, S. Glick, S. Kurtz, and J. Wohlgemuth, "Accelerated testing and modeling of potential-induced degradation as a function of temperature and relative humidity," *IEEE Journal of Photovoltaics*, vol. 5, no. 6, p. 1549–1553, 2015.
- [22] M. Gagliardi, P. Lenarda, and M. Paggi, "A reaction-diffusion formulation to simulate eva polymer degradation in environmental and accelerated ageing conditions," *Solar Energy Materials and Solar Cells*, vol. 164, p. 93–106, 2017.
- [23] B. Han and D.-S. Kim, "Moisture ingress, behavior, and prediction inside semiconductor packaging: A review," *Journal of Electronic Packaging*, 2017.
- [24] R. E. Kumar, G. V. Gastrow, J. Leslie, R. Meier, M. I. Bertoni, and D. P. Fenning, "Quantitative determination of moisture content in solar modules by short-wave infrared reflectometry," *IEEE Journal of Photovoltaics*, vol. 9, no. 6, p. 1748–1753, 2019.
- [25] C. Shen, H. Kampwerth, M. Green, T. Trupke, J. Carstensen, and A. Schütt, "Spatially resolved photoluminescence imaging of essential silicon solar cell parameters and comparison with cello measurements," *Solar Energy Materials and Solar Cells*, vol. 109, p. 77–81, 2013.
- [26] N. Otsu, "A threshold selection method from gray-level histograms," *IEEE transactions on systems, man, and cybernetics*, vol. 9, no. 1, p. 62–66, 1979.
- [27] A. M. Jeffries, T. Nietzold, L. T. Schelhas, and M. I. Bertoni, "Corrosion of novel reactive silver ink and commercial silver-based metallizations in diluted acetic acid," *Solar Energy Materials and Solar Cells*, vol. 223, p. 110900, 2021.
- [28] H. B. Mann and D. R. Whitney, "On a test of whether one of two random variables is stochastically larger than the other," *The annals of mathematical statistics*, p. 50–60, 1947.
- [29] I. Duer, J. Bierbaum, J. Metzger, J. Richter, and D. Philipp, "Silver grid finger corrosion on snail track affected pv modules—investigation on degradation products and mechanisms," *Energy Procedia*, vol. 98, p. 74–85, 2016.
- [30] A. M. Jeffries and M. I. Bertoni, "Reactive silver ink as a novel low-temperature metallization: Monitoring corrosion," in *Reactive Silver Ink as a Novel Low-Temperature Metallization: Monitoring Corrosion*, vol. 2018 IEEE 7th World Conference on Photovoltaic Energy Conversion (WCPEC)(A Joint Conference of 45th IEEE PVSC, 28th PVSEC 34th EU PVSEC). IEEE, 2018, pp. 1013–1017.
- [31] S. K. Tippabhotla, N. G. Diesta, X. Zhang, S. Sridhara, C. Stan, N. Tamura, A. A. Tay, and A. Budiman, "Thermomechanical residual stress evaluation in multi-crystalline silicon solar cells of photovoltaic modules with different encapsulation polymers using synchrotron x-ray microdiffraction," *Solar Energy Materials and Solar Cells*, vol. 193, p. 387–402, 2019.
- [32] S. Dietrich, M. Pander, M. Sander, S. H. Schulze, and M. Ebert, "Mechanical and thermomechanical assessment of encapsulated solar cells by finite-element-simulation," in *Mechanical and thermomechanical assessment of encapsulated solar cells by finite-element-simulation*, N. G. Dhere, J. H. Wohlgemuth, and K. Lynn, Eds. SPIE, 2010.
- [33] A. J. Beinert, P. Romer, M. Heinrich, M. Mittag, J. Aktaa, and D. H. Neuhaus, "The effect of cell and module dimensions on thermomechanical stress in pv modules," *IEEE Journal of Photovoltaics*, vol. 10, no. 1, p. 70–77, 2020.
- [34] F. Kraemer and S. Wiese, "Assessment of long term reliability of photovoltaic glass-glass modules vs. glass-back sheet modules subjected to temperature cycles by fe-analysis," *Microelectronics Reliability*, vol. 55, no. 5, p. 716–721, 2015.
- [35] L. Rendler, P. Romer, A. Beinert, J. Walter, S. Stecklum, A. Kraft, U. Eitner, and S. Wiese, "Thermomechanical stress in solar cells: Contact pad modeling and reliability analysis," *Solar Energy Materials and Solar Cells*, vol. 196, p. 167–177, 2019.
- [36] P. Chaturvedi, B. Hoex, and T. M. Walsh, "Broken metal fingers in silicon wafer solar cells and pv modules," *Solar Energy Materials and Solar Cells*, vol. 108, p. 78–81, 2013.
- [37] F. Kraemer, J. Seib, E. Peter, and S. Wiese, "Mechanical stress analysis in photovoltaic cells during the string-ribbon interconnection process," in *Mechanical stress analysis in photovoltaic cells during the string-ribbon interconnection process*, vol. 2014 15th International Conference on Thermal, Mechanical and Mult-Physics Simulation and Experiments in Microelectronics and Microsystems (EuroSimE). IEEE, 2014, pp. 1–7.
- [38] M. Sander and S. Dietrich, "Influence of manufacturing processes and subsequent weathering on cell cracks in pv modules," *28th EU PVSEC*, 2013.
- [39] V. Handara, I. Radchenko, S. Tippabhotla, K. R. Narayanan, G. Illya, M. Kunz, N. Tamura, and A. Budiman, "Probing stress and fracture mechanism in encapsulated thin silicon solar cells by synchrotron x-ray microdiffraction," *Solar Energy Materials and Solar Cells*, vol. 162, p. 30–40, 2017.
- [40] C. Peike, S. Hoffmann, P. Hülsmann, B. Thaidigsmann, K. A. Weiß, M. Koehl, and P. Bentz, "Origin of damp-heat induced cell degradation," *Solar Energy Materials and Solar Cells*, vol. 116, p. 49–54, 2013.
- [41] ITRPV, "International technology roadmap for photovoltaic 2020," 2020.
- [42] M. T. Zarmai, N. Ekere, C. Oduoza, and E. H. Amalu, "A review of interconnection technologies for improved crystalline silicon solar cell photovoltaic module assembly," *Applied Energy*, vol. 154, p. 173–182, 2015.